







TOOLS

Software for lattice light-sheet imaging of FRET biosensors, illustrated with a new Rap1 biosensor

Ellen C. O'Shaughnessy¹, Orrin J. Stone¹, Paul K. LaFosse¹ , Mihai L. Azoitei¹, Denis Tsygankov^{1,6} , John M. Heddleston² , Wesley R. Legant³, Erika S. Wittchen⁴ , Keith Burridge⁴ , Timothy C. Elston¹, Eric Betzig³, Teng-Leong Chew², David Adalsteinsson⁵, and Klaus M. Hahn¹ 

Lattice light-sheet microscopy (LLSM) is valuable for its combination of reduced photobleaching and outstanding spatiotemporal resolution in 3D. Using LLSM to image biosensors in living cells could provide unprecedented visualization of rapid, localized changes in protein conformation or posttranslational modification. However, computational manipulations required for biosensor imaging with LLSM are challenging for many software packages. The calculations require processing large amounts of data even for simple changes such as reorientation of cell renderings or testing the effects of user-selectable settings, and lattice imaging poses unique challenges in thresholding and ratio imaging. We describe here a new software package, named ImageTank, that is specifically designed for practical imaging of biosensors using LLSM. To demonstrate its capabilities, we use a new biosensor to study the rapid 3D dynamics of the small GTPase Rap1 in vesicles and cell protrusions.

Introduction

Lattice light-sheet microscopy (LLSM) provides a unique combination of capabilities. It can rapidly produce a series of fluorescence images with a resolution up to $220 \times 220 \times 370$ nm, and with photobleaching significantly reduced relative to other 3D fluorescence imaging methods (Chen et al., 2014). LLSM has already produced greatly enhanced views of multiple cell and organism behaviors (Strom et al., 2017; Valm et al., 2017; McArthur et al., 2018). Using LLSM together with fluorescent biosensors could extend its capabilities even further, revealing not only protein localization but also the activity of proteins in real time. Biosensor imaging can quantify the dynamics of diverse activation events, including conformational changes, phosphorylation events, cleavage, and binding interactions (Goguen and Imperiali, 2011; Mehta and Zhang, 2011; Zhang et al., 2018). Quantifying biosensor activity does, however, require extensive image processing, which is especially challenging for LLSM due to the tremendous volume of data generated by this technique, and the computationally intensive steps required to quantitate protein activity from biosensor data. This led us to develop LLSM-specific scripts in the graphical programming language DataTank (<https://www.visualdatatools.com>), whose highly efficient architecture was well suited to

the challenges of LLSM imaging. Initial success with this approach spurred us to develop new image processing software, ImageTank, to incorporate the efficiencies inherent in this programming language into user-friendly graphical user interfaces to quantify and visualize biosensor activity in 3D over time. These scripts were developed specifically for LLSM data, but are adaptable to other imaging modalities.

To harness the capabilities of LLSM, we developed a new biosensor for the small GTPase Rap1. Rap1 coordinates very diverse cellular processes and is thought to mediate communication between integrin engagement at the ventral surface and distant dynamics ruffles (Arthur et al., 2004; Takahashi et al., 2008; Miyata et al., 2009). Using rapid 3D visualization of Rap1 activity, we quantified simultaneous Rap1 regulation at these different localizations and identified connections between activation on the ventral surface and in peripheral ruffles.

Results

We developed a dual-chain (intermolecular Förster resonance energy transfer [FRET]) biosensor for Rap1 (Rap1 fluorescent activity reporter [FLARE]) consisting of Rap1 N-terminally fused

¹Department of Pharmacology, University of North Carolina at Chapel Hill, Chapel Hill, NC; ²Advanced Imaging Center, Janelia Research Campus, Howard Hughes Medical Institute, Ashburn, VA; ³Janelia Research Campus, Howard Hughes Medical Institute, Ashburn, VA; ⁴Department of Cell Biology and Physiology, University of North Carolina at Chapel Hill, Chapel Hill, NC; ⁵Department of Mathematics, University of North Carolina at Chapel Hill, Chapel Hill, NC; ⁶Department of Biomedical Engineering, Georgia Institute of Technology and Emory University, Atlanta, GA.

Correspondence to David Adalsteinsson: david@unc.edu; Klaus M. Hahn: khahn@med.unc.edu; P.K. LaFosse's present address is National Institutes of Mental Health, Bethesda, MD; W.R. Legant's present address is Departments of Pharmacology and Biomedical Engineering, University of North Carolina at Chapel Hill, Chapel Hill, NC; E. Betzig's present address is Department of Physics, University of California, Berkeley, Berkeley, CA.

© 2019 O'Shaughnessy et al. This article is distributed under the terms of an Attribution–Noncommercial–Share Alike–No Mirror Sites license for the first six months after the publication date (see <http://www.rupress.org/terms/>). After six months it is available under a Creative Commons License (Attribution–Noncommercial–Share Alike 4.0 International license, as described at <https://creativecommons.org/licenses/by-nc-sa/4.0/>).

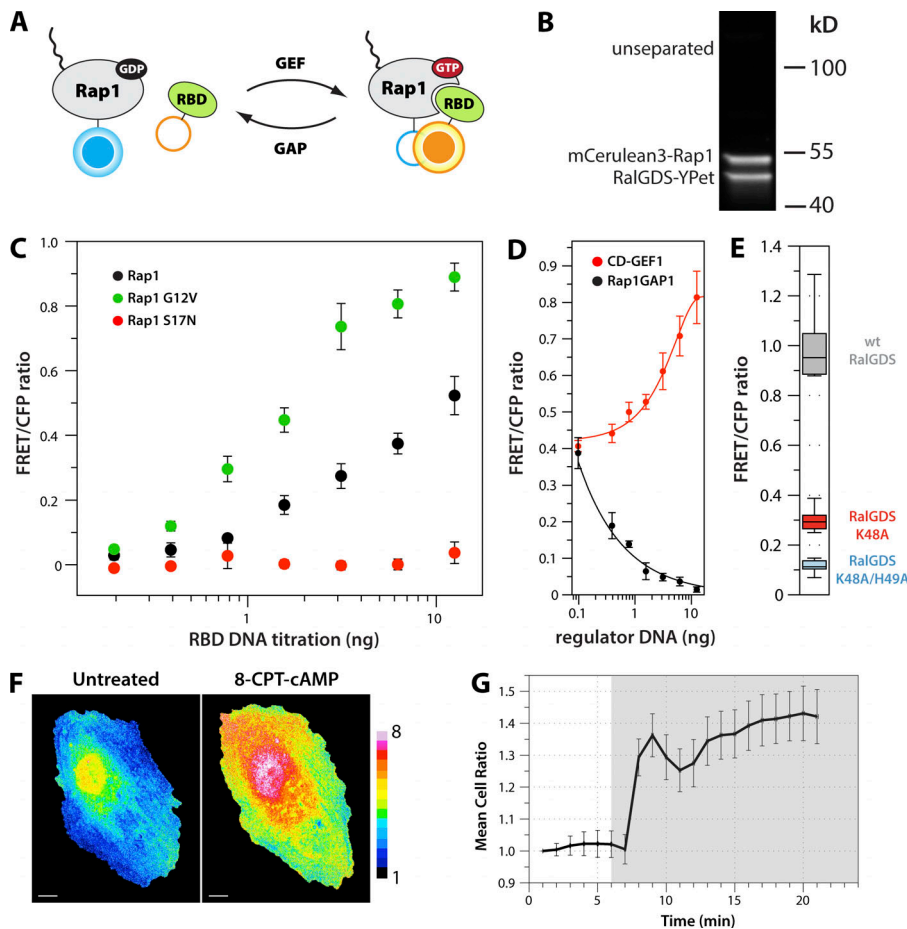


Figure 1. Rap1 biosensor. (A) Schematic of the Rap1 biosensor showing that FRET occurs when GTP-loaded Rap1 binds the RBD, bringing mCerulean3 (blue) and YPet (yellow) together. (B) Representative Western blot showing separation of both components of the biosensor, expressed using tandem viral 2A sequences. (C) Measuring the FRET response of the biosensor by titrating the RBD component with a constant concentration of constitutively active (G12V), dominant-negative (S17N), and WT Rap1. Results are from 12 (WT and S17N) or 13 (G12V) replicates of the full titration. Error is the SEM. There is no detectable FRET for the S17N mutant. This together with high FRET efficiency yielded a sensitive biosensor. All plate assays were performed with LinXe cells. (D) The biosensor reported activation when expressed with CalDAG-GEF1 and inactivation when coexpressed with Rap1GAP1. Results from $n = 5$ distinct replicates are shown. Error is the SEM. (E) FRET was greatly reduced by introducing either a K48A or K48A/H49A mutations into the RalGDS affinity reagent to abrogate binding (box and whisker plot, $n = 12$). (F) Individual frames of Rap1 biosensor activity in HUVECs with (right panel) and without (left panel) stimulation by a small molecule activator of Epac, a Rap1 GEF (8-CPT-cAMP). Scale bars, 10 μm . (G) HUVECs expressing the biosensor were stimulated with 8-CPT-cAMP (shown in gray), and the mean cell ratio was normalized to 1 at the first time point ($n = 6$ cells, error is the SEM).

to the acceptor fluorophore, mCerulean3 (Markwardt et al., 2011), and the Rap1-binding domain (RBD) of the effector protein RalGDS fused to the acceptor fluorophore YPet (Nguyen and Daugherty, 2005; Fig. 1 A). Use of dual-chain biosensors can be complicated by cell-to-cell variation in the relative expression level of the two chains. To overcome this, we developed an optimized viral 2A sequence that expressed both proteins from a single mRNA, greatly reducing variability in the relative stoichiometry of the sensor chains (Fig. 1 B). Rap1 FLARE was validated by testing the interaction of constitutively active and dominant negative mutants (Fig. 1 C), its response to native regulators (Fig. 1 D), effects of mutations that alter RBD-Rap1 interaction (Fig. 1 E), and responses in live cells (Fig. 1, F and G). Importantly, the dual-chain design yielded zero FRET in the off-state, which, in combination with bright fluorophores, resulted in a sensitive reporter of activity, and simplified placement of fluorophores to maximize FRET efficiency. Using this biosensor, we imaged Cos7 cells as they migrated over fibronectin-coated coverslips. We acquired 199 slices per cell and, for each slice, we collected FRET (donor excitation/acceptor emission) and CFP simultaneously on two complementary metal-oxide-semiconductor (sCMOS) cameras, and then collected YFP for bleedthrough correction (Fig. 2). The total acquisition time per time point was ~ 8 s, and we acquired 90–180 whole cell activity maps in 11.8–24.2 min, comprising up to 30 GB of data per cell.

Because of the large amounts of data that had to be manipulated to produce biosensor images in 3D, it was important to handle data efficiently. We needed to use an approach that would not repeat calculations whenever the user changed routine visualization parameters (e.g., rotation, exposed slice, or scaling). The scripts we generated therefore stored intermediate results in memory to avoid repeated evaluations, and automatically cleared results when inputs changed. If an input had not changed, the program returned the saved result rather than recomputing complex tasks. Functional tasks were categorized based on their run-time complexity, the relative sizes of input/output data, and the repetition of function calls. Based on these properties and the computational needs of the workflow, data were selected for storage either in memory (fast) or on disk (slow). This enabled us to edit parameters anywhere in the workflow and immediately visualize or analyze quantitative results without recomputing tasks not affected by that change. All image files associated with a given cell were converted into a single streamlined file that included raw data from each acquisition channel, microscope settings, configuration files, and pertinent processing information. These data were stored in large contiguous blocks to speed up reading/writing and did not have the extraneous overhead information found in standard .tif files. The scripts perform flat-field correction, registration, background subtraction, photobleach correction (Hodgson et al., 2006), bleedthrough correction, and thresholding (Fig. 2) on 4D

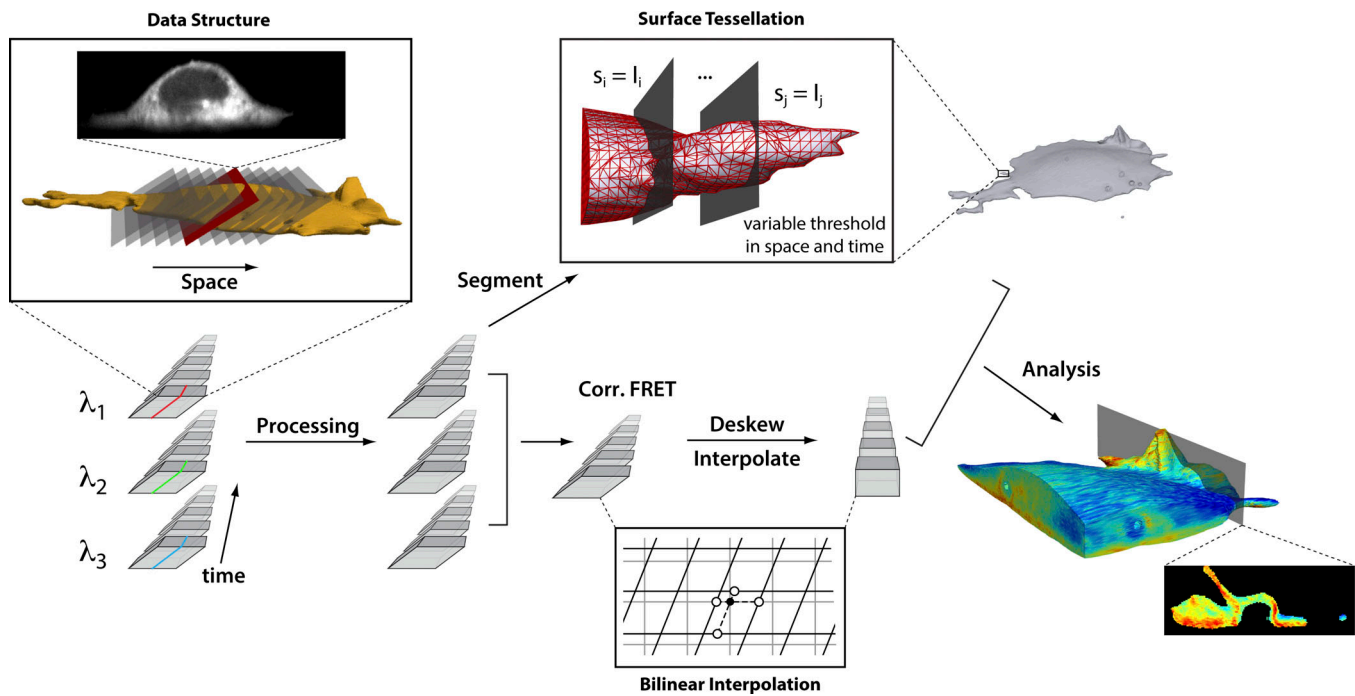


Figure 2. **Workflow for biosensor processing of LLSM data.** The software performs initial image processing steps including flat-field correction, registration, background subtraction, photobleach correction, and bleedthrough correction. Because of great variation in the intensity values at each slice, thresholding (defining the boundary of the cell) can be done manually or with a function fit to changing values specified over a series of slices and/or time points. The surface of the cell is determined through tessellation, a process in which the edge is interpolated based on the threshold values in a rolling local region. The measure of activity (e.g., the FRET ratio or total corrected FRET [Corr. FRET]) is determined for the entire field of view, and then the surface is rendered based on edge segmentation or other surfaces of interest. The advantage of this scheme is that, without additional computation, changes in segmentation can be updated immediately and multiple surfaces such as the outer edge of the cell and regions of high activity can be shown simultaneously. After the activity measures are calculated, the images are deskewed and interpolated on a user-specified grid to generate a solid 3D-cell volume. Finally, ImageTank includes scripts to analyze biosensor activity in any region of interest or in any plane through the cell and to measure these regions or objects in physically meaningful units.

biosensor data (Hodgson et al., 2010). They enable continuous replay of videos even during data manipulations, display of protein activity as a solid 3D volume that can be analyzed on any plane, and rendering of multiple surfaces or features of interest simultaneously. Further, these modular scripts can be extended to incorporate additional analysis, either through external functions encoded in python but run within ImageTank or by exporting data as .mat (MATLAB) or .xlsx (Excel) files.

After standard image corrections were performed, biosensor activity was calculated for the entire data cube, and the cell was segmented. Segmentation, or defining the cell boundary, was challenging because data cube axes are not orthogonal and resolution differs in x, y, and z. In our approach to segmentation, we assumed that there was an underlying continuous intensity function in 3D that is sampled on the scale of the voxel. The user defines threshold values for individual 2D slices to generate a function of threshold intensities across space. This threshold function was used to render a 3D cell volume via tessellation, using the marching cubes algorithm (Lorenson and Cline, 1987; Fig. S1). This procedure interpolated triangular planes between the center of the voxels to produce a complete, connected surface with subpixel accuracy. In contrast to a pixel-based segmentation method, tessellation more accurately captures the cell edge even in images with lower signal-to-noise ratios

(Fig. S2). In developing this schema, we chose to set thresholds based on the fluorescent protein YPet from the biosensor instead of using a separate membrane marker, to preserve additional fluorescence channels for future multiplexing studies. Using tessellation was essential for this process because in some parts of the cell, edges were not as clearly defined as they would be with a membrane marker, or as they are in wide-field microscopy with higher intensity images. A key advantage of LLSM is reduced photobleaching, enabling prolonged visualization of lower biosensor concentrations that do not perturb cell biology.

Automated cell segmentation was one of the most difficult challenges in working with this data. We explored histogram-based, gradient-based, and adaptive methods, but none could capture all the different features in the specimens. We were most successful using a histogram-based approach on deconvolved data, but when we mapped the resulting contours onto the nondeconvolved data, we were not confident of the overlay. Visual assessment to vary threshold values over both space and time, though tedious, was the most robust method for segmenting the cell. We are confident in the cell features we describe, as we repeatedly tested effects of different threshold values. We continue to work on automated methods to implement in future versions of the software.

Images acquired in LLSM were at an angle of 31.8° from the coverslip and had to be deskewed and interpolated to render an object with the correct dimensions and the customary orientation (Chen et al., 2014; Fig. 2). To map the 3D grid of the original image data onto a physically accurate new grid, we applied a full transformation, correcting for the angle and the physical spacing between slices, which was determined by the step size during acquisition. After deskewing, we used interpolation on a user-defined grid to generate a solid 3D object that could be analyzed on any plane. The step size in LLSM was sufficient to accurately interpolate information between slices, enabling us to measure features of interest in physical units. The user-friendly graphical user interfaces associated with each step in the process were coded as modular components that can be incorporated as needed by users and can be applied to any 4D imaging technique.

The computational approaches were developed and optimized using the Rap1 biosensor in proof of principle studies. This clearly demonstrated the power of LLSM to reveal rapid 3D dynamics, and to visualize correlations between even brief activation events across the cell. Rap1 was found to be associated with intracellular vesicles that originated from (Video 1) and fused with (Video 2) the ventral and dorsal cell membranes (Fig. 3). It was also seen in dorsal ruffles (Fig. 4 and Videos 3 and 4), in lateral protrusions (Video 5), and under the cell (Fig. S3). The cells were plated on fibronectin to stimulate integrin-induced protrusions. Consistent with previous studies indicating that Rap1 mediates integrin activation and control of protrusions (Arthur et al., 2004; Takahashi et al., 2008; Miyata et al., 2009), throughout our observations we saw Rap1 activation on large areas of the ventral cell surface. In contrast, activations within ruffles were rapid and transient, and included striking localized spikes of activity that would be difficult to characterize without the superior spatiotemporal resolution of LLSM (Fig. 4 and Videos 3 and 4). There were in some cases continuous “bridges” of activated Rap1 connecting the ventral membrane to dorsal ruffles (Video 6). Rap1 was activated in two distinct types of vesicles (Fig. 3). In 25% of the cells, we saw moving vesicles with very low Rap1 activity in their center, but a partial shell of high activity around the periphery. These vesicles (diameter, 1.2–4.4 μm), with morphology suggestive of macropinosomes, formed from either the ventral or dorsal surfaces and in some cases originated from a ruffle folding in on the cell (Video 7). 42% of the cells contained large (1.5–4.7 μm), oblong bodies, with active Rap1 throughout. These were predominantly perinuclear and were seen to rotate around the nucleus (Video 8). The sizes of these vesicles were calculated using the suite of measurement tools we developed (Fig. S4).

Discussion

In summary, we provide a tailored computational approach and user-friendly software to study biosensors with LLSM. The efficiencies that are built into these computational tools are amenable to other 4D imaging modalities as well as different biosensor designs. The power of combining LLSM with biosensors was demonstrated using a new Rap1 biosensor. We provided evidence that activated Rap1 is a messenger carrying

information from sites of integrin activation to dorsal protrusions, showed rapid dynamics of Rap1 in ruffles with complex 3D geometry, and showed different types of vesicles containing activated Rap1.

Materials and methods

Rap1 biosensor

The Rap1 biosensor was cloned into the pTriEx4 expression vector (Novagen). The Rap1 effector binding domain of RalGDS (743–830) was C-terminally tagged with the acceptor fluorophore YPet (Nguyen and Daugherty, 2005) separated by a short linker, tccgga ggatccggttctactcag. Full-length Rap1 was N-terminally tagged with the donor fluorophore mCerulean3 (Markwardt et al., 2011) separated by the linker SGLRSRAKL. We use the terms “CFP” and “YFP” in the scripts to refer, in general, to the donor and acceptor fluorescent protein variants that are commonly used in our FRET biosensors. Other names can be substituted as appropriate. Expression of both biosensor components from a single mRNA was mediated by tandem viral 2A sequences from porcine teschovirus-1 (P2A) and *Thosea asigna* virus (T2A; Kim et al., 2011) separated by a LQRPN SKKTSNSQKIN linker. Rap1 was placed downstream of the viral 2A sequence to preserve native regulation of the hypervariable region.

Biosensor validation

Biosensors were validated using a plate-based assay described previously (Slattery and Hahn, 2014). In brief, LinXE 293T cells were plated in 96-well plates and transiently transfected with appropriate constructs using lipofectamine reagent (50470; Invitrogen). Cells were incubated for 16–24 h, imaged using a 10× objective (0.3 NA; air; Olympus) with MetaMorph (Molecular Devices) control software, and analyzed with custom MATLAB (MathWorks) scripts. To measure the corrected FRET ratio for constitutively active (G12V) and dominant-negative (S17N) mutants, a fixed amount of DNA (5 ng) for expression of mCerulean3-Rap1 (WT, constitutively active, or dominant negative) was transfected along with a titration of the RalGDS-YPet over several orders of magnitude (0.19–50 ng). To enable comparison across plates acquired on different days with different microscopes, each plate contained at least two replicates of the G12V mutant, and the entire plate was normalized to the mean maximum FRET of the G12V mutant (12–13 replicates, five plates, 3 d). Error is reported as the SEM. To quantify regulation by the guanine nucleotide exchange factor (CalDAG-GEF1) and the GTPase-activating protein (Rap1GAP1), a fixed amount (10 ng) of the WT Rap1 biosensor expressed with a viral 2A sequence (see above) was transfected while the Rap1 regulator was titrated over several orders of magnitude (0.39–100 ng). Each plate was normalized to the mean maximum FRET of the CalDAG-GEF1 titration (five replicates, four plates, 2 d). Error is reported as the SEM. Point mutations known to abrogate binding of RalGDS to Rap1 (K48A, H49A) were introduced, and RalGDS(K48A/H49A)-YPet, RalGDS(K48A)-YPet, or RalGDS-YPet was titrated against a fixed amount of mCerulean3-Rap1G12V. Each plate was normalized to the mean maximum FRET of RalGDS-YPet (12 replicates, six

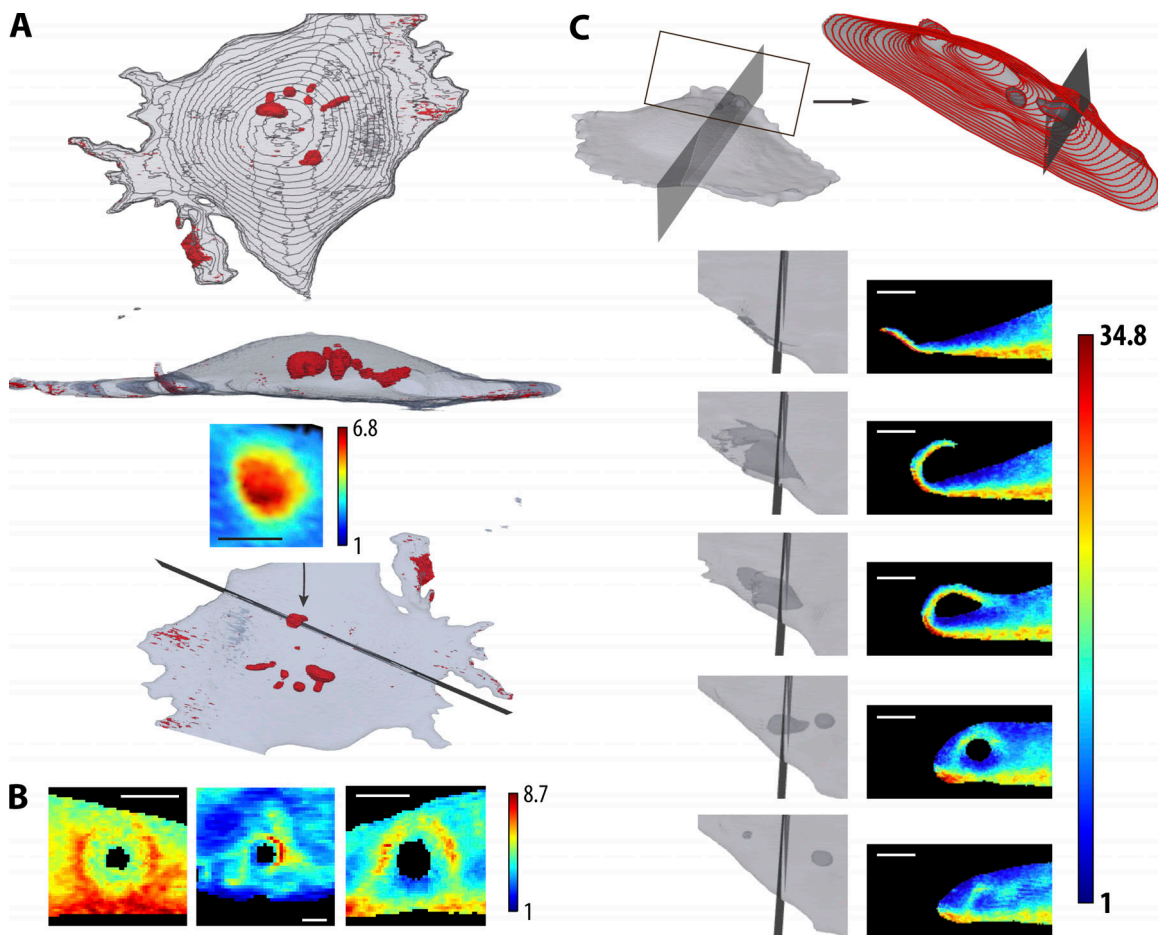


Figure 3. **Rap1 activity in different types of vesicular structures.** (A) Approximately half of the Cos7 cells exhibited high Rap1 activity that extended throughout the vesicular structures. These were concentrated around the nucleus. Color scale indicates corrected FRET/CFP, excluding the highest and lowest 2% of ratio values to eliminate spurious pixels. Scale bar, 2.5 μ m. (B) 3 of 12 cells showed structures partially surrounded by a shell of Rap1 activity. These were seen to both emerge from and fuse with the ventral and dorsal surfaces. Scale bars, 2.5 μ m. (C) The surface of a cell, and a detail drawn with topographical lines to illustrate the position of a vesicle. The time series shows a region of the cell bisected by a plane through the vesicle and the corresponding plane in a pseudo-colored map of Rap1 activity. The vesicle is formed by a dorsal ruffle fusing with the top of the cell. Scale bars, 2.5 μ m.

plates, 2 d), and the highest concentration was shown as a box and whisker plot. In the box and whisker plot, the middle of the box is the median, the edges of the box are the first and third quartiles, and the lines outside of the box are the minimum and maximum values.

Stimulation and wide field imaging of Rap1 biosensor

Human umbilical vein endothelial cells (HUVECs) were transiently transfected with the WT Rap1 biosensor and mixed 1:5 with untransfected cells to generate individually transfected cells embedded in a monolayer of endothelial cells. The monolayer was imaged on an Olympus IX81 with a sCMOS camera (Hamamatsu Orca Flash 4.0) every minute for five time points. The cells were stimulated with 100 μ M 8-CPT-cAMP and imaged for another 16 time points. Biosensor analysis was performed with custom MATLAB (MathWorks) scripts. The scaling of the biosensor images was calculated based on values ranging between the 95th percentile after stimulation and the 5th percentile before stimulation. The mean whole cell ratio for six cells and the SEM were quantified over time.

Live cell imaging with LLSM

LLSM

LLSM microscopes used in these experiments are housed in the Betzig laboratory and in the Advanced Imaged Center at the Howard Hughes Medical Institute, Janelia Research Campus. Cos7 cells were transiently transfected with biosensor plasmid 16–24 h before imaging using Fugene6 (Promega). Cells used for live cell imaging were seeded on coverslips (CS-5R; Warner Instruments) coated with 10 μ g/ml fibronectin in Leibovitz L15 Medium, no phenol red (21083027; Thermo Fisher Scientific), containing 5% FBS. The system was configured and operated as previously described (Chen et al., 2014).

Samples were illuminated at 37°C using a 445-nm diode laser (Oxxius) at 60% acousto-optic tunable filter transmittance, 50 mW initial laser power (2.75 μ W at the back focal plane), and a 488-nm diode laser (MPB Communications) at 30% acousto-optic tunable filter transmittance, 30 mW initial laser power (4.71 μ W at back focal plane) sequentially scanned on the spatial light modulator (Fourth Dimension Displays) and focused through the excitation objective (0.65 NA water immersion;

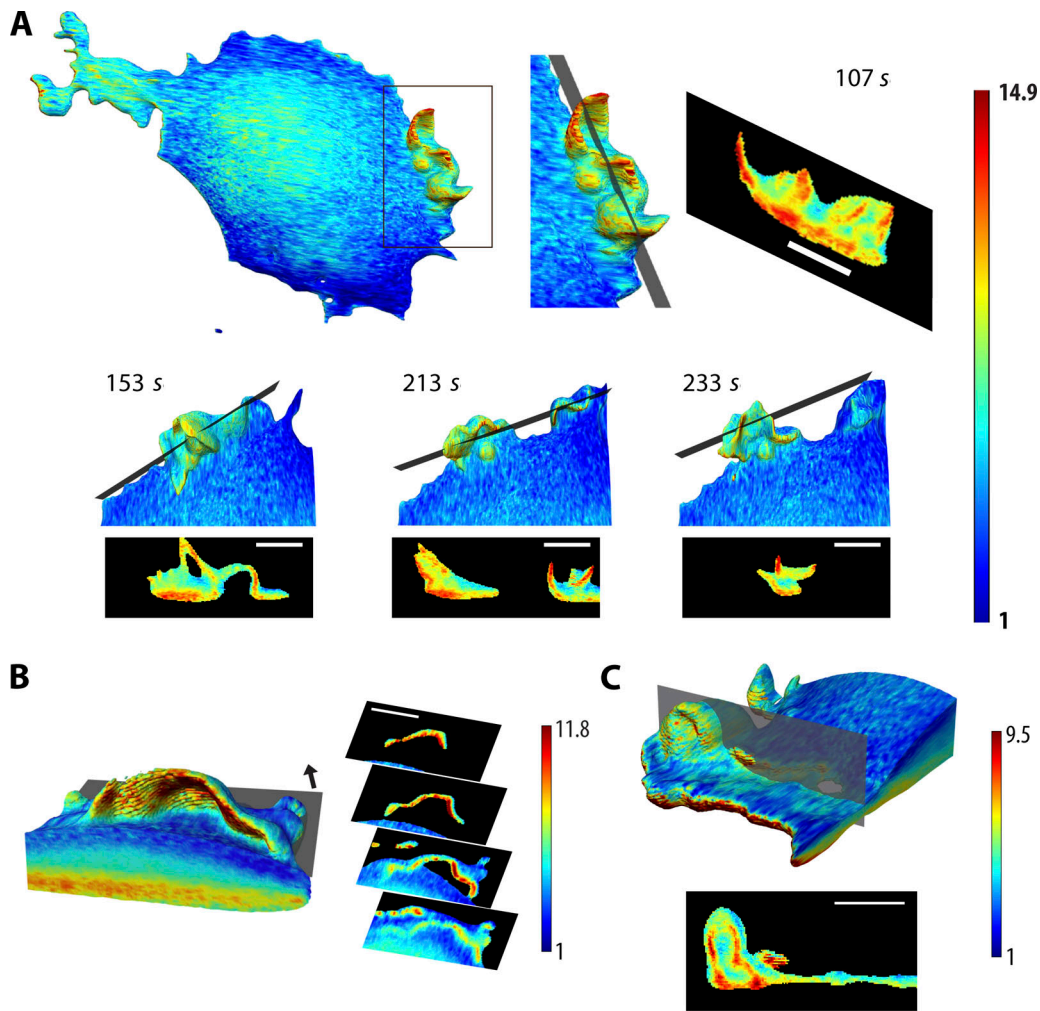


Figure 4. **Rap1 dynamics in ruffles.** (A) The ruffles at upper left (box) are cut by the planes shown at different times. Note the changing distribution of active Rap1 and Rap1 activity distributed from the ventral surface all the way to the top of the ruffles (upper right plane). Color scale indicates corrected FRET/CFP, excluding the highest and lowest 2% of ratio values to eliminate spurious pixels. Scale bars, 5 μ m. (B) A concave ruffle is cut by a series of planes parallel to the coverslip, at increasing height above the coverslip. Highest Rap1 activity is seen on the surface of the ruffle facing the direction of motion (Video 4). The shape of the ruffle is evident in the pattern of Rap1 activity on the bottom of the Cos7 cell (lowest plane). Scale bar, 5 μ m. (C) A dorsal ruffle is cut by a single plane showing Rap1 activity throughout the structure and in connections to a dense region of high activity on the bottom of the Cos7 cell. Scale bar, 5 μ m.

Special Optics). Fluorescence emission was collected by a detection objective (CFI Apo LWD 25XW, 1.1 NA; Nikon), and detected on sCMOS cameras (Hamamatsu Orca Flash 4.0 v2). Point-spread functions for each excitation wavelength were experimentally measured using 200-nm tetraspeck beads adhered to 5-mm glass coverslips (T7280; Invitrogen) as a direct measure of light-sheet and optical quality. A total of 12 cells from three time courses were acquired on two separate days: 180 time points, 8.12 s per cell volume, 24.2 min total time; 120 time points, 8.12 s per cell volume, 16.1 min total time; and 90 time points, 7.96 s per cell volume, 11.8 min total time. The software used to operate the instrument and collect data was LabView (National Instruments).

Image analysis

Biosensor processing requires several computational steps that vary depending on the biosensor in question, the imaging setup, and the experimental design. To handle these different

circumstances, a modular biosensor processing script was developed that enables the user to select optional processing steps as needed (or add additional steps if required). Further, the data from each module are stored until they are specifically altered, which allows the user to focus on a given step in the process without having to recalculate previous steps. This data management scheme facilitates rapid exploration of very large datasets. The scripts consist of modules for organizing the raw data, flat-field correction, image registration, background subtraction/photobleach correction, segmentation, bleedthrough correction, and biosensor visualization and analysis. Please note that Apple does not support NVIDIA graphics cards in their newest operating system, MacOS 10.14. This driver issue will affect some 3D rendering functions of ImageTank in older computers. Affected computers include some models from 2013 and one model from 2014, though these computers will be unaffected if running MacOS 10.13 or earlier.

Organizing the raw data

To facilitate rapid image processing, the raw .tif files were aggregated into a single contiguous data block that is read in one uninterrupted stream. The extraneous information contained in the .tif header was removed, all channels were aggregated into one file, and the image slices were organized along the y-axis for subsequent processing.

Flat-field correction

Some variation in the intensity of the excitation light-sheet is evident in LLSM and can be corrected by acquiring a flat-field image of dye during the experimental setup or by computationally determining a flat-field from a large number of datasets acquired with the same experimental conditions. To correct for variation in excitation intensity, the raw images are divided by the wavelength-specific flat-field images normalized to a mean intensity of 1.

Image registration

For simultaneous acquisition of the CFP and FRET channels, two cameras were used and registration was required to ensure that these images were properly aligned. To perform registration, we acquired images of beads that fluoresce in both the CFP and FRET channels (T7280; Invitrogen) so that the same bead could be acquired with both cameras. We identified the same beads in each image, found their centers, and used those points to generate a transform to map the CFP images to the FRET images. We used a full transformation allowing for shift, rotation, and scale, though we include an option for perspective transformation if desired. The distance between each bead pair and the mean distance of all pairs are plotted to show the goodness of fit and to facilitate selection of the optimum transform.

Background subtraction and photobleach correction

To perform both corrections, we set a rough threshold to define the cell edge. Pixels outside the threshold were considered background, and the median background intensity of each channel was subtracted from that channel. For pixels inside the cell, the sum intensity in each channel was plotted over time. A decay curve was fit to this data and used to correct for photobleaching (Hodgson et al., 2008, 2010). Each channel was divided by the appropriate decay curve normalized by the initial value.

Segmentation

We chose to segment the cell based on a component of the biosensor (RalGDS-YPet), to decrease the number of images required at each time point, and to leave channels free for multiplexing. We needed to use different threshold values for each slice as slices with low cytosolic content were dimmer than those in the middle of the cell. For each cell, a threshold value was set every 5 μm and a function was fit between the specified values. Additional slices were specified if needed to accommodate large changes, and for some cells, threshold values were adjusted over time because the cell body moved significantly. Using the function fit to the specified values, we divided each image in the YFP stack by the threshold value assigned to that image and interpolated a surface along values equal to 1.

Bleedthrough correction

Some biosensor designs, including the dual-chain (intermolecular) biosensor used here, require bleedthrough correction. Measuring bleedthrough coefficients has been described in detail previously (Hodgson et al., 2010). The α coefficient quantifies bleedthrough from the donor into the acceptor channel, and the β coefficient quantifies bleedthrough from direct excitation of the acceptor fluorophore. The bleedthrough coefficients were used to calculate the corrected FRET (corrected FRET = FRET - $\alpha \times \text{CFP} - \beta \times \text{YFP}$) and the activity ratio (corrected FRET/CFP). Both corrected FRET and the activity ratio were calculated for the entire data cube once, and were then displayed on the full surface of the cell, on a region of the cell, in a 2D slice, or in an additional mask as desired by the user.

Code availability

ImageTank software and scripts can be obtained at <https://visualdatatools.com/ImageTank/>.

ImageTank scripts are also available for download on the Hahn Laboratory website.

Online supplemental material

A demonstration of 3D surface rendering using tessellation via the marching cubes algorithm is shown in Fig. S1. A comparison of the error associated with segmentation by either interpolation or masking is shown in Fig. S2. Views of the dorsal and ventral surfaces of several cells can be seen in Fig. S3. They reveal broad regions of high activity along the bottom of the cells. Demonstration of the measurement tool used to quantify the size of internal structures is shown in Fig. S4. Video 1 shows a vesicle emerging from the ventral cell membrane. Video 2 shows a vesicle fusing with the ventral cell membrane. Video 3 shows Rap1 activation within the ruffle. Video 4 shows Rap1 activation within the ruffle. Video 5 shows high Rap1 activity in protrusions viewed from the bottom of the cell. Video 6 shows a moving cross-section of a ruffle at a single time point. Note that the activity underlying the ruffle extends at some points to the ventral surface. Video 7 shows a vesicle formed by a folding ruffle. Video 8 shows that internal regions of high activity rotate counter-clockwise.

Acknowledgments

We thank the National Institutes of Health (R35GM122596 and R01HL133668) and the U.S. Department of Defense (W911NF-15-1-0631/A16-0438-001) for their support. The Advanced Imaging Center is jointly sponsored by the Howard Hughes Medical Institute and the Gordon and Betty Moore Foundation.

The authors declare no competing financial interests.

Author contributions: E.C. O'Shaughnessy produced the Rap1 biosensor and spearheaded the experimental work. E.S. Wittchen and K. Burridge contributed to live cell testing of the biosensor. K.M. Hahn initiated and supervised the project. E.C. O'Shaughnessy, D. Adalsteinsson, and K.M. Hahn wrote the paper with input from all authors. D. Adalsteinsson wrote the software with assistance from P.K. LaFosse, and with input from K.M. Hahn and E.C. O'Shaughnessy. T.L. Chew and

J.M. Heddleston provided the LLSM instrument at the Janelia Farm Advanced Imaging Center, and helped with experiments there. W.R. Legant carried out LLSM studies in the Betzig laboratory together with E.C. O’Shaughnessy and M.L. Azoitte, under the direction of E. Betzig. O.J. Stone and M.L. Azoitte carried out initial biosensor studies, and D. Tsygankov carried out the initial development of software and the data analysis approach.

Submitted: 4 March 2019

Revised: 28 June 2019

Accepted: 25 July 2019

References

- Arthur, W.T., L.A. Quilliam, and J.A. Cooper. 2004. Rap1 promotes cell spreading by localizing Rac guanine nucleotide exchange factors. *J. Cell Biol.* 167:111–122. <https://doi.org/10.1083/jcb.200404068>
- Chen, B.C., W.R. Legant, K. Wang, L. Shao, D.E. Milkie, M.W. Davidson, C. Janetopoulos, X.S. Wu, J.A. Hammer III, Z. Liu, et al. 2014. Lattice light-sheet microscopy: imaging molecules to embryos at high spatiotemporal resolution. *Science*. 346:1257998. <https://doi.org/10.1126/science.1257998>
- Goguen, B.N., and B. Imperiali. 2011. Chemical tools for studying directed cell migration. *ACS Chem. Biol.* 6:1164–1174. <https://doi.org/10.1021/cb200299k>
- Hodgson, L., P. Nalbant, F. Shen, and K. Hahn. 2006. Imaging and photobleach correction of Mero-CBD, sensor of endogenous Cdc42 activation. *Methods Enzymol.* 406:140–156. [https://doi.org/10.1016/S0076-6879\(06\)06012-5](https://doi.org/10.1016/S0076-6879(06)06012-5)
- Hodgson, L., O. Pertz, and K.M. Hahn. 2008. Design and optimization of genetically encoded fluorescent biosensors: GTPase biosensors. *Methods Cell Biol.* 85:63–81. [https://doi.org/10.1016/S0091-679X\(08\)85004-2](https://doi.org/10.1016/S0091-679X(08)85004-2)
- Hodgson, L., F. Shen, and K. Hahn. 2010. Biosensors for characterizing the dynamics of rho family GTPases in living cells. *Curr. Protoc. Cell Biol.* 14:1–26. <https://doi.org/10.1002/0471143030.cb1411s46>
- Kim, J.H., S.R. Lee, L.H. Li, H.J. Park, J.H. Park, K.Y. Lee, M.K. Kim, B.A. Shin, and S.Y. Choi. 2011. High cleavage efficiency of a 2A peptide derived from porcine teschovirus-1 in human cell lines, zebrafish and mice. *PLoS One*. 6:e18556. <https://doi.org/10.1371/journal.pone.0018556>
- Loresen, W.E., and H.E. Cline. 1987. Marching cubes: A high resolution 3D surface construction algorithm. *ACM SIGGRAPH Computer Graphics* 21:163–169. <https://doi.org/10.1145/37402.37422>
- Markwardt, M.L., G.J. Kremers, C.A. Kraft, K. Ray, P.J.C. Cranfill, K.A. Wilson, R.N. Day, R.M. Wachter, M.W. Davidson, and M.A. Rizzo. 2011. An improved cerulean fluorescent protein with enhanced brightness and reduced reversible photoswitching. *PLoS One*. 6:e17896. <https://doi.org/10.1371/journal.pone.0017896>
- McArthur, K., L.W. Whitehead, J.M. Heddleston, L. Li, B.S. Padman, V. Oorschot, N.D. Geoghegan, S. Chappaz, S. Davidson, H. San Chin, et al. 2018. BAK/BAX macropores facilitate mitochondrial herniation and mtDNA efflux during apoptosis. *Science*. 359:eaao6047. <https://doi.org/10.1126/science.aao6047>
- Mehta, S., and J. Zhang. 2011. Reporting from the field: genetically encoded fluorescent reporters uncover signaling dynamics in living biological systems. *Annu. Rev. Biochem.* 80:375–401. <https://doi.org/10.1146/annurev-biochem-060409-093259>
- Miyata, M., Y. Rikitake, M. Takahashi, Y. Nagamatsu, Y. Yamauchi, H. Ogita, K. Hirata, and Y. Takai. 2009. Regulation by afadin of cyclical activation and inactivation of Rap1, Rac1, and RhoA small G proteins at leading edges of moving NIH3T3 cells. *J. Biol. Chem.* 284:24595–24609. <https://doi.org/10.1074/jbc.M109.016436>
- Nguyen, A.W., and P.S. Daugherty. 2005. Evolutionary optimization of fluorescent proteins for intracellular FRET. *Nat. Biotechnol.* 23:355–360. <https://doi.org/10.1038/nbt1066>
- Slattery, S.D., and K.M. Hahn. 2014. A High-Content Assay for Biosensor Validation and for Examining Stimuli that Affect Biosensor Activity. *Curr. Protoc. Cell Biol.* 65:1–31. <https://doi.org/10.1002/0471143030.cb1415s65>
- Strom, A.R., A.V. Emelyanov, M. Mir, D.V. Fyodorov, X. Darzacq, and G.H. Karpen. 2017. Phase separation drives heterochromatin domain formation. *Nature*. 547:241–245. <https://doi.org/10.1038/nature22989>
- Takahashi, M., Y. Rikitake, Y. Nagamatsu, T. Hara, W. Ikeda, K. Hirata, and Y. Takai. 2008. Sequential activation of Rap1 and Rac1 small G proteins by PDGF locally at leading edges of NIH3T3 cells. *Genes Cells*. 13:549–569. <https://doi.org/10.1111/j.1365-2443.2008.01187.x>
- Valm, A.M., S. Cohen, W.R. Legant, J. Melunis, U. Hershsberg, E. Wait, A.R. Cohen, M.W. Davidson, E. Betzig, and J. Lippincott-Schwartz. 2017. Applying systems-level spectral imaging and analysis to reveal the organelle interactome. *Nature*. 546:162–167. <https://doi.org/10.1038/nature22369>
- Zhang, J., S. Mehta, and C. Schultz. 2018. *Optical probes in biology*. CRC Press, Boca Raton, FL.